

ARTICLE

Open Access

Multiple-patterning colloidal lithography-implemented scalable manufacturing of heat-tolerant titanium nitride broadband absorbers in the visible to near-infrared

Dasol Lee¹, Myeongcheol Go², Minkyung Kim¹, Junho Jang², Chungryong Choi², Jin Kon Kim^{2,3} and Junsuk Rho^{1,2,3}

Abstract

Broadband perfect absorbers have been intensively researched for decades because of their near-perfect absorption optical property that can be applied to diverse applications. Unfortunately, achieving large-scale and heat-tolerant absorbers has been remained challenging work because of costly and time-consuming lithography methods and thermolability of materials, respectively. Here, we demonstrate a thermally robust titanium nitride broadband absorber with >95% absorption efficiency in the visible and near-infrared region (400–900 nm). A relatively large-scale (2.5 cm × 2.5 cm) absorber device is fabricated by using a fabrication technique of multiple-patterning colloidal lithography. The optical properties of the absorber are still maintained even after heating at the temperatures >600 °C. Such a large-scale, heat-tolerant, and broadband near-perfect absorber will provide further useful applications in solar thermophotovoltaics, stealth, and absorption controlling in high-temperature conditions.

Introduction

Broadband perfect absorbers^{1–8} have many possible uses, such as thermophotovoltaics^{9–11} and thermal emitters^{12–14}, but practical applications have been limited by the lack of scalable fabrication method and by their poor thermal durability. Broadband perfect absorbers are typically realized by plasmonic nanostructures bonded to metallic reflective layer separated by a dielectric spacer in which noble metals are commonly used^{1,15}, but these materials are costly. Therefore, refractory materials have been introduced as candidates for broadband absorbers

due to their high-temperature tolerance, chemical stability, mechanical durability, and low cost^{16–20}.

Titanium nitride (TiN) has comparable plasmonic properties to gold (Au) in the visible and near-infrared (NIR) region, and has therefore been used in solar heat generators and photodetectors^{21–24}. However, most previous studies have used electron beam lithography to pattern the nanostructures, and this method limits a scale to a few hundred micrometers. To be implemented in practical applications, a method to fabricate TiN nanostructure in a large scale is in high demand.

Colloidal lithography is widely used to create periodic 2D nano-sized patterns on a variety of substrates. It can fabricate templates or masks for use in creation of various nanostructures, such as nanohole, nanodisk, nanopillar, and nanocone, which have been applied to various photonic devices^{25–28}. A consecutive use of the colloidal lithography, which is referred to as multiple-patterning colloidal lithography (MPCL), enables fabrication of hierarchical

Correspondence: Jin Kon Kim (jkkim@postech.ac.kr) or Junsuk Rho (jsrho@postech.ac.kr)

¹Department of Mechanical Engineering, Pohang University of Science and Technology (POSTECH), Pohang 37673, Republic of Korea

²Department of Chemical Engineering, Pohang University of Science and Technology (POSTECH), Pohang 37673, Republic of Korea

Full list of author information is available at the end of the article
These authors contributed equally: Dasol Lee, Myeongcheol Go

© The Author(s) 2021



Open Access This article is licensed under a Creative Commons Attribution 4.0 International License, which permits use, sharing, adaptation, distribution and reproduction in any medium or format, as long as you give appropriate credit to the original author(s) and the source, provide a link to the Creative Commons license, and indicate if changes were made. The images or other third party material in this article are included in the article's Creative Commons license, unless indicated otherwise in a credit line to the material. If material is not included in the article's Creative Commons license and your intended use is not permitted by statutory regulation or exceeds the permitted use, you will need to obtain permission directly from the copyright holder. To view a copy of this license, visit <http://creativecommons.org/licenses/by/4.0/>.

nanostructures, such as hollow nanocone, nanotower, and nanoring^{29–34}. However, these methods have only been used to etch silicon or polymers, while not being extended to etch other materials.

Here, we use MPCL to fabricate a large-scale (2.5 cm × 2.5 cm) near-perfect absorber that is composed of ring-shaped TiN structures. To best of our knowledge, it is the first demonstration of applying MPCL to etch a refractory metal, which is focused on the fabrication approach to overcome the limitations of practical use as a large-scale absorber. The device has polarization-independent absorption of 95.4% under normal incidence and high absorption at incident angles up to $\theta = 40^\circ$ at visible and NIR wavelength ($400 < \lambda < 900$ nm). The near-perfect absorption of our device remains even after heating at temperature up to 600 °C. We expect that our cost-effective and scalable absorber is a promising candidate for large-scale applications, such as photothermal devices and thermal emitters that require polarization-independent, angle-insensitive, heat-tolerant, and broadband absorption.

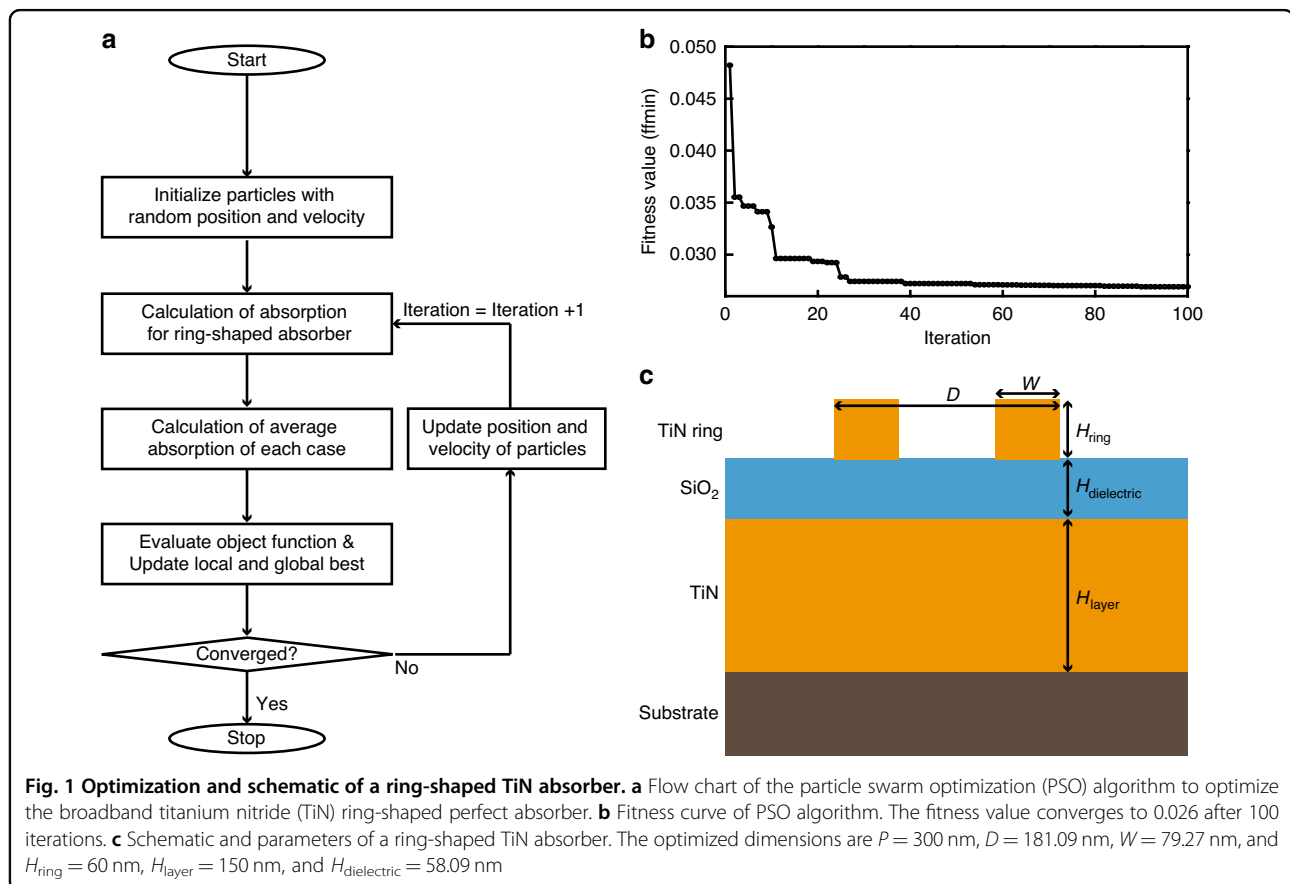
Results and discussion

Device optimization and fabrication

The proposed broadband ring-shaped TiN absorber has a metal–insulator–metal (MIM) structure that uses a

perfectly-reflective TiN layer, silicon dioxide (SiO₂) dielectric layer, and a top composed of ring-shaped TiN nanostructures in a hexagonal array. The ring-shaped nanostructure has advantages in absorption due to its better impedance matching with air compared to disk-shaped structures^{16,19}, and can be fabricated in large scale using MPCL.

Particle swarm optimization (PSO)³⁵ is used to optimize the structural parameters of the TiN absorber to have the highest absorption in the visible and NIR region. For this purpose, we develop a lab-built PSO by linking commercial software (COMSOL Multiphysics 5.5, Livelink for MATLAB, MATLAB 2019; Fig. 1a). First, finite-element method simulation is performed to calculate the absorption from randomly selected initial parameters. The objective function indicates the function to be optimized, and is defined by subtracting the square of the average absorption in 400–900 nm region from unity. Then the optimization proceeds to minimize the fitness value of this objective function. At each iteration, minimum fitness value is set as the local best. If the new local best is smaller than the minimum fitness value in history (global best), the local best is set as the new global best. The cycle is repeated until fitness converges or until the maximum number of iterations is applied.



The outer diameter (D) and width (W) of the ring structure of the top ring-shaped nanostructure, and the thickness ($H_{\text{dielectric}}$) of the SiO_2 dielectric layer are considered as parameters for optimization, and other parameters such as period (P) and thickness of ring structure (H_{ring}) are fixed due to the feasible fabrication for a TiN absorber. The initial ranges of parameters are set to $0 < D < 300$ nm and $10 < W < 150$ nm to prevent them from exceeding the outer diameter. One hundred iterations are repeated until the optimal value is found. Each iteration considers 30 particles, so a total of 3000 particles are evaluated to identify the final parameters for optimal ring-shaped absorber. After 100 iterations, the fitness converges to < 0.026 (Fig. 1b).

The optimal dimensions of the proposed ring-shaped TiN absorber (Fig. 1c) are $P = 300$ nm in a hexagonal array, $D = 181.09$ nm, $W = 79.27$ nm, and $H_{\text{ring}} = 60$ nm on the layers deposited by TiN ($H_{\text{layer}} = 150$ nm) and SiO_2 ($H_{\text{dielectric}} = 58.09$ nm) in sequence. As such, optimization techniques can help in designing optical structures and can be further advanced using machine learning or deep learning^{36–40}.

Schematic illustration to fabricate the TiN ring-shaped absorber is described (Fig. 2a). TiN– SiO_2 –TiN MIM structure is prepared on silicon substrate, then MPCL is used to prepare highly ordered TiN ring-shaped

structures; the period and diameters are determined by controlling the size of the polystyrene (PS) nanosphere and the oxygen plasma etching time. A PS monolayer is firstly prepared on the top layer of the prepared MIM structure (Fig. 2b). PS nanospheres with a diameter of 300 nm are chosen to match the period between nanoring structures. The hexagonally arranged PS monolayer is etched using oxygen plasma to reduce the PS diameter to the optimized D . A top TiN layer is etched using reactive ion etching (RIE) with Cl_2 and BCl_3 gas by using the PS beads as a mask. The RIE yields a nanodisk structure, then a second PS etching is performed to achieve the optimized W (Fig. 2c). A 8-nm thick nickel (Ni) layer is deposited as a hard mask under Cl_2 gas using electron beam (e-beam) evaporator; then all remaining PS nanospheres are removed by sonication in toluene for an hour. The second TiN etching is performed (Fig. 2d). The Ni mask is removed by 1 mol/L HCl solution to complete the final TiN nanoring structure. These processes yields ring-shaped nanostructure array that is consistent with the optimized parameters (Fig. 2e). In order to fabricate elaborate nanostructure, there are several issues to be considered. First, the etching conditions must be precisely controlled⁴¹ because the intrinsic property of dry etching process can make the ring-shaped structure slightly tapered. Second, the uniformity of the structure can be

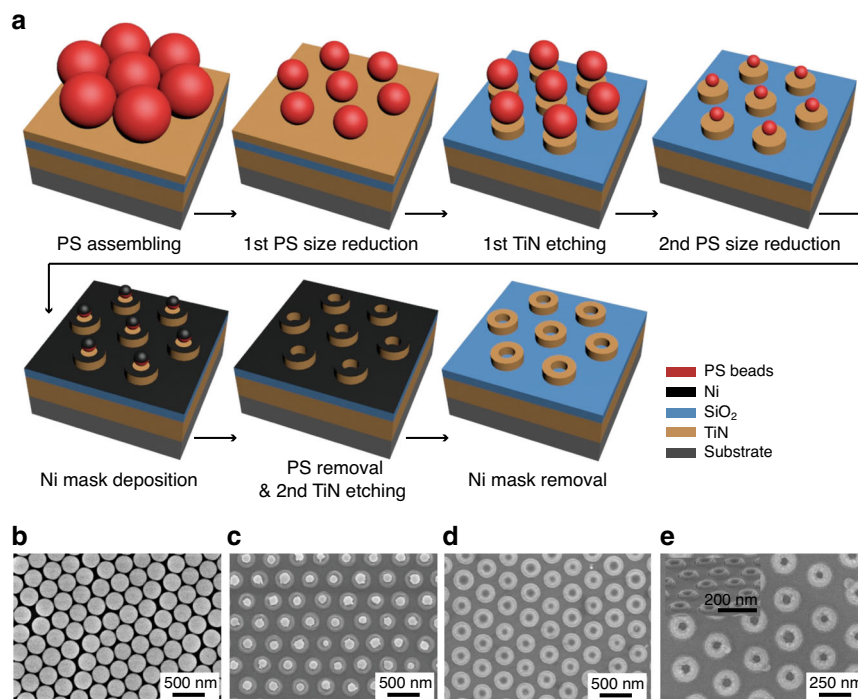


Fig. 2 Fabrication of a ring-shaped TiN absorber. Hexagonally patterned TiN absorber with multiple-patterning colloidal lithography (MPCL). **a** Schematic illustration of the process. Highly ordered TiN ring-shaped structures are fabricated using MPCL. Scanning electron microscopy images **b** of hexagonally packed PS nanospheres monolayer, **c** after second PS size reduction, **d** after PS removal, **e** of final ring-shaped TiN absorber. Inset shows the tilted view of final ring-shaped TiN absorber

improved by using nanospheres with lower size distribution. Third, random tilting of the etched PS nanospheres during the RIE etching can be prevented by enhancing the adhesion between PS nanospheres and TiN layer by heating³¹.

Optical properties

For numerical demonstration, we calculate absorption of the ring-shaped TiN absorber; refractive indices of TiN and SiO₂ are taken from the literature^{42–44}. The result shows 95.9% average absorption at 400–900 nm and the highest absorption at 650 nm (Fig. 3a). High absorption of the proposed design is experimentally demonstrated using spectroscopy. Unpolarized light is illuminated at normal incidence onto the sample. The measured spectra of ring-shaped absorber and MIM structure (Fig. 3a) show an average absorption of 95.4%. Compared to the MIM layer without ring-shaped structure, it absorbs >31% light in the visible–NIR region. The slight difference between measurement and simulation is attributed to fabrication imperfections of placement and size distributions of the nanostructure. Photographs (Fig. 3a, inset) of ring-shaped absorber and MIM structure show obvious darkness obtained by the absorption characteristic.

To understand the mechanism of the high absorption, we examine the total power dissipation density

$$Q_{\text{abs}} = \langle J \cdot E \rangle = \rho |E|^2 = \frac{1}{2} \epsilon_0 \epsilon_r'' \omega |E|^2 \quad (1)$$

where ρ is the electrical conductivity, ϵ_0 is the permittivity of a vacuum, ϵ_r'' is the imaginary part of the relative permittivity of the material, ω is angular frequency, and $|E|$ is the amplitude of the total electric field inside the material. Q_{abs} is extracted from each TiN layer. Q_{abs} can be a criterion to evaluate the contribution of the absorbed electromagnetic power from each TiN layer.

Absorption can be explained as a field localization by localized surface plasmons (LSPs) and by intrinsic loss of the material. The absorption contributions of each TiN layer verify the specific mechanisms (Fig. 3b). The LSPs occur at the surface near the nanostructures, so the absorption by the LSP should be caused by the ring-shaped nanostructure. In the region of $\lambda > 600$ nm, TiN exhibits metallic properties, which lead to plasmonic resonance. Thus, the absorption is dominated by the ring structure. However, compared to noble metals, such as Au, TiN has weak metallic properties, so it has localized fields inside the ring structure. In addition, unlocalized waves can pass through the top layer and arrive at the underlying TiN bulk layer due to its large skin depth. The broad high absorption is attributed to two absorptions in the ring structure and bulk TiN layers simultaneously. In the range of $\lambda < 600$ nm, the bottom TiN layer contributes more absorption than the ring structure does. This difference means that the intrinsic loss at the bulk TiN layer is dominant. TiN can be a lossy dielectric material in this region, so the bottom TiN layer absorbs a large portion of incident light at high frequencies.

For further investigation, the impedance-matching condition of the proposed absorber is analyzed. Under the assumptions that the absorber structures are homogeneous, the effective impedance (Fig. 4a) of the proposed structure is retrieved using the S-parameter retrieval method as⁴⁵

$$z = \pm \sqrt{\frac{(1 + S_{11})^2 - S_{21}^2}{(1 - S_{11})^2 - S_{21}^2}} \quad (2)$$

The effective impedance is calculated under the condition of plane wave from air. The effective impedance shows the real part of the calculated effective impedance is close to 1, and the imaginary part is close to 0, so the

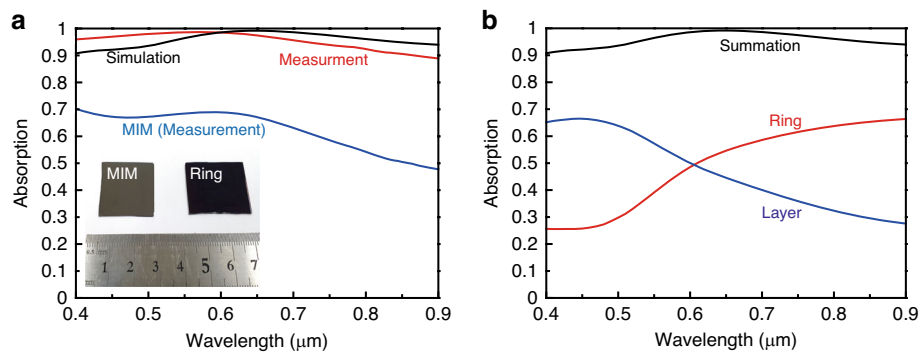
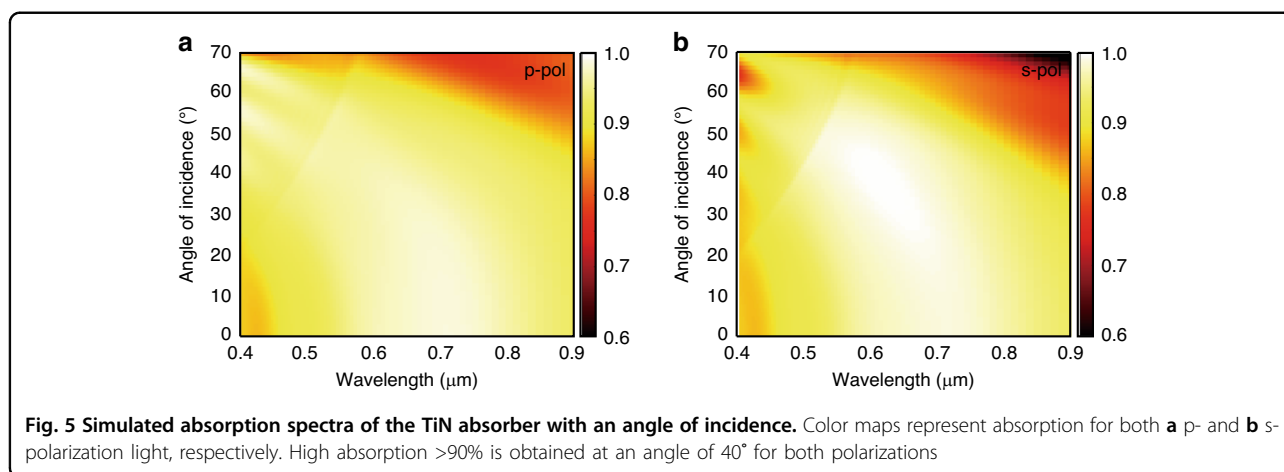
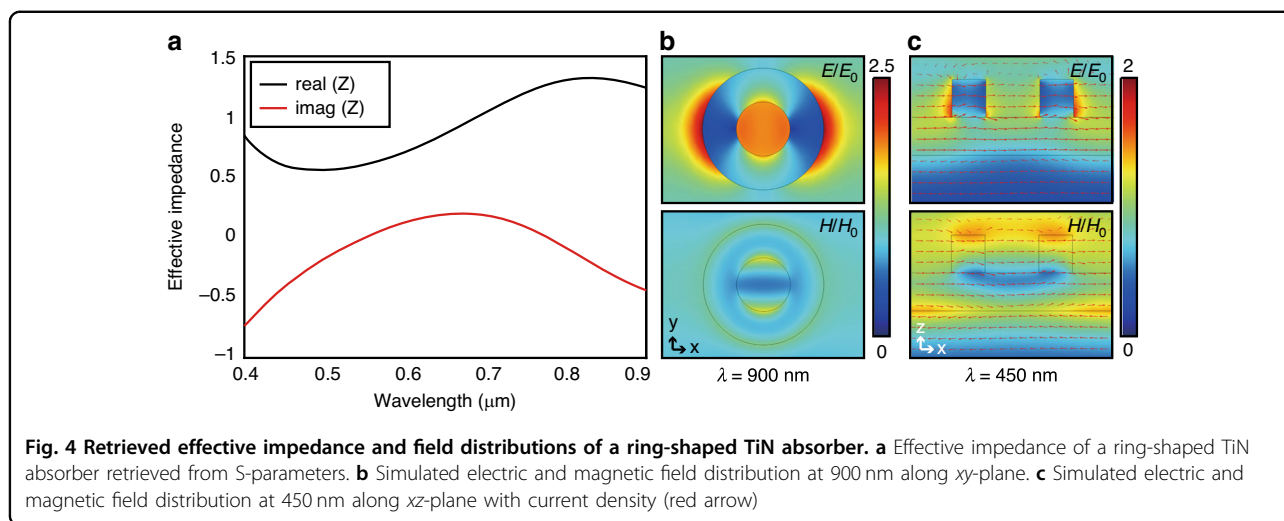


Fig. 3 Absorption spectrum and the total power dissipation density. **a** Simulated (black line) and measured (red line) absorption spectra of ring-shaped absorber and measured absorption spectrum of metal–insulator–metal (MIM) structure (blue line) for comparison. Inset: photographs of fabricated absorbers. **b** The total power dissipation density of top ring-shaped TiN nanostructure array (red line), bottom TiN layer (blue line) to examine absorption contribution of two TiN layers. The summation of two dissipation densities (black line) is equal to the simulated absorption spectrum



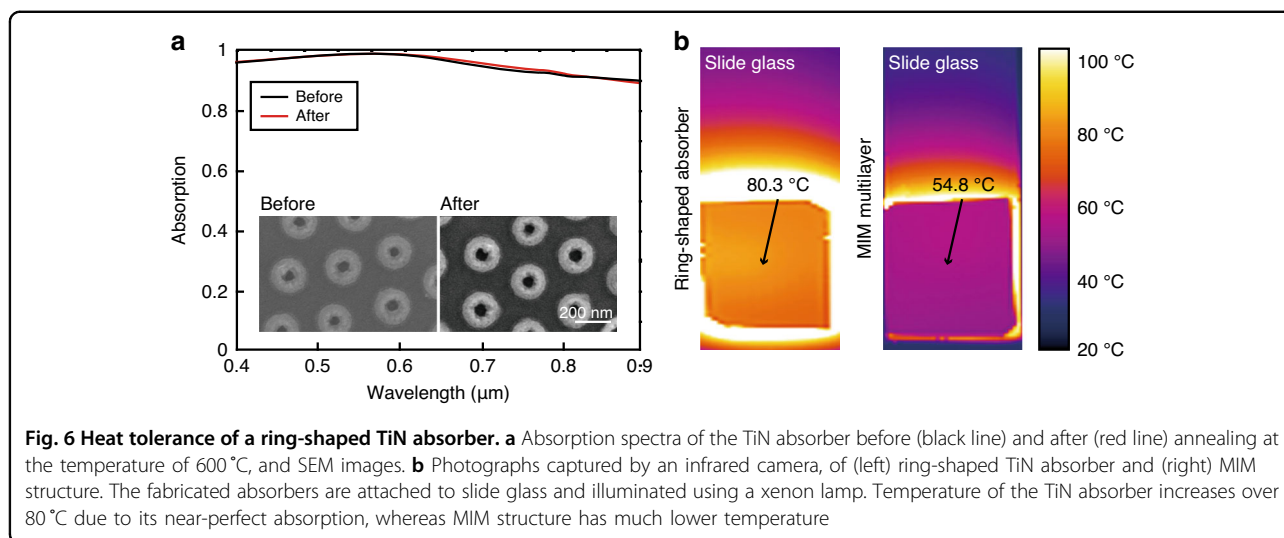
impedance matches that of free space in the visible and NIR regions. Thus, reflection is weak and absorption is dominant over the desired wavelength region.

Normalized plots of electric and magnetic field distribution on the xy - and xz -planes are plotted in Fig. 4b, c. We analyze the fields at $\lambda = 900$ nm and $\lambda = 450$ nm, which are the resonance peaks in TiN ring and layer, respectively (Fig. 3b). At $\lambda = 900$ nm, the electric field distribution shows an electric dipole resonance at the top ring antenna, whereas the magnetic field distribution is relatively weak. This result demonstrates that the absorption is mainly caused by the ring-shaped nanostructure. In contrast, at $\lambda = 450$ nm, the magnetic field distribution shows a magnetic dipole resonance as a result of coupling between the TiN layers. The anti-parallel current density J_d leads a loop bringing an artificial magnetic dipole moment. Thus, the ring-shaped TiN absorber excites electric and magnetic resonances, which increase the localized electromagnetic field at the corresponding wavelength.

The ring-shaped absorber is radially symmetrical, so its absorption is not greatly affected by polarization or incident angle of light at $\theta < 40^\circ$ (Fig. 5a, b). However, at $\theta > 40^\circ$, absorption decreases because the confinement of the EM field weakens. This degradation occurs because the resonances are sensitive to polarization and incident angle. Nevertheless, our observation confirms that absorption $>90\%$ is maintained at an angle of 40° in both p- and s-polarizations. This characteristic means that the proposed absorber can be widely used in practical fields, such as photothermal applications.

Heat tolerance

The proposed absorber is expected to have a great heat tolerance as a result of TiN's high melting point of 2930°C . To confirm the heat tolerance of the ring-shaped TiN absorber, it is heated in a vacuum chamber at 600°C for 6 h and cooled down to room temperature. We confirm that the TiN absorber maintains its shape and optical properties even after heating at high temperature (Fig. 6a).



Even at a high temperature near 600 °C, TiN and SiO₂ show only slight changes in their permittivities, but each retains its original optical properties quite well^{46,47}. If the TiN absorber is protected by an atomic layer deposited coating or sealing, it may tolerate even much higher temperatures¹⁶.

For practical applications such as solar and photovoltaic fields, we test the photothermal stability of the TiN absorber under natural-like condition in an open environment. White light from a high-power xenon lamp is collimated and illuminated at fabricated samples that are fixed on slide glass. The sample is far enough from the source to avoid a direct thermal effect by the high temperature of the lamp. MIM structure is measured and compared to the TiN absorber for the photothermal activity. After being illuminated for same duration (5 min), the temperature of each sample is captured using an infrared camera (Testo 885, Testo; Fig. 6b). The temperature of the TiN absorber increases to >80 °C, which is 25.5 °C higher than that of MIM structure. The high absorption in our devices, combined with the ring-shaped nanostructure opens a gateway for efficient energy extraction in photothermal applications, due to advantages of low-cost and compatibility with large-scale fabrication.

Conclusion

We have reported a large-scale heat-tolerant TiN broadband absorber that shows >95% of unpolarized light absorption in the visible–NIR range of 400 < λ < 900 nm. We propose the implementation of cost-effective MPCL with refractory metal for fabrication of a centimeter scale ring-shaped absorber. Because of the heat-tolerant characteristic, the TiN absorber retains high absorption after heating up to 600 °C. This absorber will find wide applications in solar thermophotovoltaics, stealth,

and further absorption controlling in high-temperature conditions.

Materials and methods

Materials

Suspensions of PS nanospheres with 0.3- μ m diameter were used (Thermo Fisher Scientific). Absolute ethanol and toluene were used (Sigma Aldrich). Deionized water was obtained from a water purification system (Ultima Duo 300, Azzota Scientific). Hydrochloric acid (1 mol/L) was used (Samchun Chemical).

Fabrication

TiN and SiO₂ layers of MIM were deposited using DC Sputtering and e-beam evaporator. The PS colloidal monolayer were self-assembled into hexagonally closed-packed arrays on the TiN layer by using an air interface method. The diameters of the PS nanospheres were reduced by oxygen RIE (VITA, Femto Science) at 80 W with 30 sccm O₂. The top TiN layer was first etched at 100 W with 25 sccm Cl₂ and 100 sccm BCl₃. Then a second PS etching was performed in the same conditions. Then an 8-nm thick Ni layer was deposited by e-beam evaporator at a deposition rate of 0.3 Å/s. Then, the PS nanospheres were removed by sonication in toluene. A second TiN etching was performed in the same condition as the first etching. Finally, the Ni mask was easily removed by immersion in 1 mol/L hydrochloric acid for 10 min, followed by rinsing with DI water.

Characterization

A UV–VIS–NIR spectrometer (Cary 5000, Varian Co.) with diffuse reflectance accessory (Internal DRA-2055, Varian Co.) was used to characterize the absorption of the large-area sample in the wavelength range 400–900 nm, using white reflectance standards (Ocean optics) as a

reference. The wavelength-sampling step was 1 nm. We defined absorption as 1-reflectance.

Fabricated TiN absorber structures were observed using a scanning electron microscope (Hitachi S4800) at 3 kV.

The thermal images were taken by an infrared camera (Testo 885, Testo), and the temperature was determined using Testo IRsoft software. The emissivity of 0.34 and room temperature of 21 °C were used for calibration. For calibration, we used an approach to directly measure the emissivity value of the infrared camera using a contact thermometer.

Acknowledgements

This work was financially supported by the National Research Foundation (NRF) grants (NRF-2019R1A2C3003129, CAMM-2019M3A6B3030637, NRF-2019R1A5A8080290, NRF-2018M3D1A1058997) funded by the Ministry of Science and ICT (MSIT), Republic of Korea. J.K.K. acknowledges the National Creative Research Initiative Program (NRF-2013R1A3A2042196) funded by the NRF-MSIT, Republic of Korea. M.K. acknowledges the NRF Global Ph.D. fellowship (NRF-2017H1A2A1043204) funded by the Ministry of Education, Republic of Korea.

Author details

¹Department of Mechanical Engineering, Pohang University of Science and Technology (POSTECH), Pohang 37673, Republic of Korea. ²Department of Chemical Engineering, Pohang University of Science and Technology (POSTECH), Pohang 37673, Republic of Korea. ³National Institute of Nanomaterials Technology (NINT), Pohang 37673, Republic of Korea

Author contributions

J.R., J.K.K., D.L. and M.G. initiated and developed the idea. D.L. and M.K. performed numerical simulations. D.L. and M.G. performed experiments. D.L., M.G., M.K., J.J., C.C., J.K.K. and J.R. prepared the manuscript. J.R. and J.K.K. supervised the research. All authors participated in the discussion and approved the final manuscript.

Conflict of interest

The authors declare that they have no conflict of interest.

Received: 1 September 2020 Revised: 19 November 2020 Accepted: 29 December 2020

Published online: 02 March 2021

References

- Aydin, K., Ferry, V. E., Briggs, R. M. & Atwater, H. A. Broadband polarization-independent resonant light absorption using ultrathin plasmonic super absorbers. *Nat. Commun.* **2**, 1–7 (2011).
- Mattiucci, N., Bloemer, M., Aközbeek, N. & D'aguanno, G. Impedance matched thin metamaterials make metals absorbing. *Sci. Rep.* **3**, 1–11 (2013).
- Cui, Y. et al. Ultrabroadband light absorption by a sawtooth anisotropic metamaterial slab. *Nano Lett.* **12**, 1443–1447 (2012).
- Sturmborg, B. C. et al. Total absorption of visible light in ultrathin weakly absorbing semiconductor gratings. *Optica* **3**, 556–562 (2016).
- Zhu, L. et al. Angle-selective perfect absorption with two-dimensional materials. *Light Sci. Appl.* **5**, e16052–e16052 (2016).
- Riley, C. T. et al. Near-perfect broadband absorption from hyperbolic metamaterial nanoparticles. *Proc. Natl Acad. Sci. USA*. **114**, 1264–1268 (2017).
- Lin, H. et al. A 90-nm-thick graphene metamaterial for strong and extremely broadband absorption of unpolarized light. *Nat. Photonics* **13**, 270–276 (2019).
- Lee, D. et al. Polarization-sensitive tunable absorber in visible and near-infrared regimes. *Sci. Rep.* **8**, 1–7 (2018).
- Lenert, A. et al. A nanophotonic solar thermophotovoltaic device. *Nat. Nanotechnol.* **9**, 126–130 (2014).
- Wang, Z. et al. Dynamic tuning of optical absorbers for accelerated solar-thermal energy storage. *Nat. Commun.* **8**, 1–9 (2017).
- Zhou, L. et al. Self-assembled spectrum selective plasmonic absorbers with tunable bandwidth for solar energy conversion. *Nano Energy* **32**, 195–200 (2017).
- Huang, J. et al. Harnessing structural darkness in the visible and infrared wavelengths for a new source of light. *Nat. Nanotechnol.* **11**, 60–66 (2016).
- Liu, X. et al. Taming the blackbody with infrared metamaterials as selective thermal emitters. *Phys. Rev. Lett.* **107**, 045901 (2011).
- Chen, X., Chen, Y., Yan, M. & Qiu, M. Nanosecond photothermal effects in plasmonic nanostructures. *ACS Nano* **6**, 2550–2557 (2012).
- Massiot, I. et al. Metal nanogrid for broadband multiresonant light-harvesting in ultrathin GaAs layers. *ACS Photonics* **1**, 878–884 (2014).
- Kim, I., So, S., Rana, A. S., Mehmood, M. Q. & Rho, J. Thermally robust ring-shaped chromium perfect absorber of visible light. *Nanophotonics* **7**, 1827–1833 (2018).
- Zhao, F., Qiao, J. & Zhang, Z. Tungsten nanoring perfect absorber for solar thermophotovoltaic system. In *Frontiers in Optics, FTH2A-5* (Optical Society of America, San Jose, California, 2015).
- Rana, A. S., Mehmood, M. Q., Jeong, H., Kim, I. & Rho, J. Tungsten-based ultrathin absorber for visible regime. *Sci. Rep.* **8**, 1–8 (2018).
- Li, W. et al. Refractory plasmonics with titanium nitride: broadband metamaterial absorber. *Adv. Mater.* **26**, 7959–7965 (2014).
- Deng, H. et al. Broadband perfect absorber based on one ultrathin layer of refractory metal. *Opt. Lett.* **40**, 2592–2595 (2015).
- Kaur, M., Ishii, S., Shinde, S. L. & Nagao, T. All-ceramic solar-driven water purifier based on anodized aluminum oxide and plasmonic titanium nitride. *Adv. Sustain. Syst.* **3**, 1800112 (2019).
- Ishii, S., Sugavaneshwar, R. P. & Nagao, T. Titanium nitride nanoparticles as plasmonic solar heat transducers. *J. Phys. Chem. C* **120**, 2343–2348 (2016).
- Hussain, A. A., Sharma, B., Barman, T. & Pal, A. R. Self-powered broadband photodetector using plasmonic titanium nitride. *ACS Appl. Mater. Interfaces* **8**, 4258–4265 (2016).
- Guler, U. et al. Local heating with lithographically fabricated plasmonic titanium nitride nanoparticles. *Nano Lett.* **13**, 6078–6083 (2013).
- Wu, Z. & Zheng, Y. Moiré chiral metamaterials. *Adv. Opt. Mater.* **5**, 1700034 (2017).
- Zhou, Z. et al. Broad-range electrically tunable plasmonic resonances of a multilayer coaxial nanohole array with an electroactive polymer wrapper. *ACS Appl. Mater. Interfaces* **9**, 35244–35252 (2017).
- Wang, J., Duan, G., Li, Y., Liu, G. & Cai, W. Wet etching-assisted colloidal lithography: a general strategy toward nanodisk and nanohole arrays on arbitrary substrates. *ACS Appl. Mater. Interfaces* **6**, 9207–9213 (2014).
- Teng, F. et al. Precise regulation of tilt angle of Si nanostructures via metal-assisted chemical etching. *Nanoscale* **9**, 449–453 (2017).
- Ai, B., Yu, Y., Mohwald, H., Wang, L. & Zhang, G. Resonant optical transmission through topologically continuous films. *ACS Nano* **8**, 1566–1575 (2014).
- Fang, X. et al. Hierarchically ordered silicon metastructures from improved self-assembly-based nanosphere lithography. *ACS Appl. Mater. Interfaces* **12**, 12345–12352 (2020).
- Xu, X. et al. Multiple-patterning nanosphere lithography for fabricating periodic three-dimensional hierarchical nanostructures. *ACS Nano* **11**, 10384–10391 (2017).
- Jeong, S., McGehee, M. D. & Cui, Y. All-back-contact ultra-thin silicon nanocone solar cells with 13.7% power conversion efficiency. *Nat. Commun.* **4**, 1–7 (2013).
- Chen, Z. et al. Synergistic effects of plasmonics and electron trapping in graphene short-wave infrared photodetectors with ultrahigh responsivity. *ACS Nano* **11**, 430–437 (2017).
- Im, H. et al. Self-assembled plasmonic nanoring cavity arrays for SERS and LSPR biosensing. *Adv. Mater.* **25**, 2678–2685 (2013).
- Kennedy, J. & Eberhart, R. Particle swarm optimization. In *Proceedings of ICNN'95-International Conference on Neural Networks*, Vol. 4, 1942–1948. (IEEE, Perth, WA, 1995).
- So, S., Badloe, T., Noh, J., Rho, J. & Bravo-Abad, J. Deep learning enabled inverse design in nanophotonics. *Nanophotonics* **9**, 1041–1057 (2020).
- So, S., Mun, J. & Rho, J. Simultaneous inverse design of materials and structures via deep learning: demonstration of dipole resonance engineering using core-shell nanoparticles. *ACS Appl. Mater. Interfaces* **11**, 24264–24268 (2019).
- So, S. & Rho, J. Designing nanophotonic structures using conditional deep convolutional generative adversarial networks. *Nanophotonics* **8**, 1255–1261 (2019).

39. Sajedian, I., Lee, H. & Rho, J. Design of high transmission color filters for solar cells directed by deep Q-learning. *Sol. Energy* **195**, 670–676 (2020).
40. Sajedian, I., Badloe, T. & Rho, J. Optimisation of colour generation from dielectric nanostructures using reinforcement learning. *Opt. Express* **27**, 5874–5883 (2019).
41. Okada, N. et al. Formation of distinctive structures of GaN by inductively-coupled-plasma and reactive ion etching under optimized chemical etching conditions. *AIP Adv.* **7**, 065111 (2017).
42. Naik, G. V., Shalaev, V. M. & Boltasseva, A. Alternative plasmonic materials: beyond gold and silver. *Adv. Mater.* **25**, 3264–3294 (2013).
43. Naik, G. V., Kim, J. & Boltasseva, A. Oxides and nitrides as alternative plasmonic materials in the optical range. *Opt. Mater. Express* **1**, 1090–1099 (2011).
44. Malitson, I. H. Interspecimen comparison of the refractive index of fused silica. *J. Opt. Soc. Am.* **55**, 1205–1209 (1965).
45. Smith, D., Vier, D., Koschny, T. & Soukoulis, C. Electromagnetic parameter retrieval from inhomogeneous metamaterials. *Phys. Rev. E* **71**, 036617 (2005).
46. Briggs, J. A. et al. Temperature-dependent optical properties of titanium nitride. *Appl. Phys. Lett.* **110**, 101901 (2017).
47. Gong, J. et al. Temperature dependent optical constants for SiO₂ film on Si substrate by ellipsometry. *Mater. Res. Express* **4**, 085005 (2017).